AGU100 ADVANCING EARTH AND SPACE SCIENCE

JGR

Journal of Geophysical Research: Planets

RESEARCH ARTICLE
10.1029/2018JE005652

Key Points:
- We measure diameters of craters associated with cold spots. Their size-frequency distribution indicates cold spots survive a few hundred kyr
- The distribution of cold spots reflects the Moon's synchronous rotation with cold spots focused on the apex of motion
- The largest cold spots with source craters larger than 800 m are concentrated on the trailing side of the moon

Supporting Information:
- Supporting Information S1
- Figure S1
- Table S1

Correspondence to:
J.-P. Williams,
jpierre@mars.ucla.edu

Citation:
Williams, J.-P., Bandfield, J. L., Paige, D. A., Powell, T. M., Greenhagen, B. T., Taylor, S., et al. (2018). Lunar cold spots and crater production on the moon. *Journal of Geophysical Research: Planets*, *123*, 2380–2392. https://doi.org/10.1029/2018JE005652

Received 20 APR 2018
Accepted 14 AUG 2018
Accepted article online 25 AUG 2018
Published online 19 SEP 2018

Author Contributions:
Conceptualization: J.-P. Williams, J. L. Bandfield, D. A. Paige, T. M. Powell, B. T. Greenhagen, S. Taylor, P. O. Hayne, R. R. Ghent, E. S. Costello
Data curation: J. L. Bandfield
Formal analysis: J.-P. Williams, T. M. Powell, S. Taylor
Funding acquisition: J.-P. Williams
Investigation: J.-P. Williams, J. L. Bandfield, B. T. Greenhagen, S. Taylor, P. O. Hayne, E. S. Costello
Supervision: J.-P. Williams
Visualization: J.-P. Williams
(continued)

Lunar Cold Spots and Crater Production on the Moon

J.-P. Williams[1], J. L. Bandfield[2], D. A. Paige[1], T. M. Powell[1], B. T. Greenhagen[3], S. Taylor[1], P. O. Hayne[4], E. J. Speyerer[5], R. R. Ghent[6], and E. S. Costello[7,8]

[1]Earth, Planetary, and Space Sciences, University of California, Los Angeles, CA, USA, [2]Space Science Institute, Boulder, CO, USA, [3]Applied Physics Laboratory, Johns Hopkins University, Laurel, MD, USA, [4]Department of Astrophysical & Planetary Sciences, University of Colorado, Boulder, Boulder, CO, USA, [5]School of Earth and Space Exploration, Arizona State University, Tempe, AZ, USA, [6]Earth Sciences, University of Toronto, Toronto, ON, Canada, [7]Department of Geology and Geophysics, University of Hawai'i at Mānoa, Honolulu, HI, USA, [8]Hawaii Institute of Geophysics and Planetology, Honolulu, HI, USA

Abstract Mapping of lunar nighttime surface temperatures has revealed anomalously low nighttime temperatures around recently formed impact craters on the Moon. The thermophysically distinct "cold spots" provide a way of identifying the most recently formed impact craters. Over 2,000 cold spot source craters were measured with diameters ranging from 43 m to 2.3 km. Comparison of the crater size-frequency distribution with crater chronology models and crater counts of superposed craters on the ejecta of the largest cold spot craters constrains the retention time of the cold spots to no more than ~0.5–1.0 Myr with smaller cold spots possibly retained for only few hundred kyr. This would suggest a relatively rapid impact gardening rate with regolith overturn depths exceeding ~5 cm over this time scale. We observe a longitudinal heterogeneity in the cold spot distribution that reflects the Moon's synchronous rotation with a higher density of cold spots at the apex of motion. The magnitude of the asymmetry indicates the craters formed from a population of objects with low mean encounter velocities ~8.4 km/s. The larger cold spots ($D > 800$ m) do not follow this trend, and are concentrated on the trailing farside. This could result from a shorter retention time for larger cold spots on the leading hemisphere due to the greater number of smaller, superposed impacts. Alternatively, the abundance of large cold spots on the trailing farside resulted from a swarm of 100-m-scale impactors striking the Moon within the last ~0.5 Myr.

Plain Language Summary Impact craters on the Moon modify the surfaces around them, resulting in patches of colder nighttime surface temperatures. These "cold spots" fade over time. Using the cold spots as markers to identify the most recent impacts that have occurred on the Moon, we measured the diameters of all the craters with cold spots. Comparing the population of these craters with the expected impact rate, we estimate that the cold spots fade over a few hundred thousand years. The cold spots are also concentrated on the western hemisphere due to the Moon's synchronous rotation where the western half of the Moon always faces toward the direction of motion of the Moon orbiting the Earth. This suggests that a relatively slow population of objects impacted the Moon in the last few hundred thousand years. The largest cold spots, however, are concentrated on the trailing hemisphere. This could result either from more small impacts on the leading hemisphere destroying larger cold spots and leaving a higher number of large cold spots on the trailing hemisphere, or a swarm of 100-m-sized objects colliding on the trailing side during this time period.

1. Introduction

A new class of small, fresh impact craters has been recently identified on the Moon through the systematic mapping of lunar surface temperatures (Bandfield et al., 2011) by the Diviner Lunar Radiometer instrument aboard the Lunar Reconnaissance Orbiter (LRO) (Paige et al., 2010; Vondrak et al., 2010). These craters are distinguished by anomalously low nighttime temperatures at distances ~10–100 crater radii from the crater centers (Figure 1). Lunar nighttime surface temperatures are characterized by sensible heat stored in the subsurface during the day radiated to space and therefore are sensitive to the thermophysical properties of the near-surface regolith to a depth of the diurnal thermal wave, ~40 cm (Hayne et al., 2017; Vasavada et al., 1999, 2012; Williams, Paige, et al., 2017). These thermophysically distinct surfaces, or "cold spots," which were initially observed by the Infrared Scanning Radiometer aboard the Apollo 17 Command-Service Module (Mendell & Low, 1974, 1975), indicate that impacts modify the surrounding regolith surfaces, making them highly insulating with little evidence for either significant deposition or erosion of surface material

Writing - original draft: J.-P. Williams
Writing – review & editing: J. L. Bandfield, D. A. Paige, T. M. Powell, P. O. Hayne, R. R. Ghent, E. S. Costello

(Bandfield et al., 2014). Cold spots appear to be common to all recent impacts and degrade relatively rapidly in the lunar space environment. Therefore, cold spots provide a means of uniquely identifying the most recent impact craters on the Moon, and thus yield information on the recent production of lunar impact craters.

2. Data and Methods

Cold spots were identified and cataloged by Bandfield et al. (2014) using 128-ppd rock-free nighttime regolith temperature maps (Bandfield et al., 2011) derived from gridded brightness temperatures of Diviner's thermal infrared spectral observations (Williams et al., 2016). Cold spot identification was limited to latitudes equatorward of ±50° as sloped surfaces at high latitudes, especially in the highland terrains, have significant temperature variations resulting from variable solar heating of the surface that render the identification of cold spots difficult. We surveyed this catalog containing 2,060 cold spot locations for source craters. A total of 2,282 craters associated with cold spots were identified including 222 new cold spots that were not in the Bandfield et al. (2014) study (Table S1). The crater diameters were measured using Lunar Reconnaissance Orbiter Camera (LROC) Narrow Angle Camera (NAC) and Wide-Angle Camera (WAC) images (Robinson et al., 2010). Approximately 6.7% of the craters either lacked NAC coverage or existing NAC images possessed low incidence angles, making the location of the crater rim difficult to discern within the immature, high reflectance material excavated by the impact event. Crater diameter estimates in these locations were based on WAC images or constrained based on the areal extent of the bright, immature regolith. Additionally, five cold spots, representing 0.22% of the cold spots surveyed, had potential source craters entirely within shadowed areas within NAC images and could not be directly measured. These craters were too small to be reliably identified in WAC images and were approximated indirectly from the size of their cold spot assuming their cold spot extended 20 crater radii from the crater. The results are insensitive to these craters as they are few in number and small in size.

Since the initial survey of cold spots published by Bandfield et al. (2014), Hayne et al. (2017) have globally mapped the thermophysical properties of the regolith fines of the Moon at 128 ppd, showing spatial variations. Modeling by Vasavada et al. (2012) found that the cooling rate of nighttime brightness temperatures observed by Diviner were closely fit with an exponentially increasing density and thermal conductivity with depth characterized by an average *e*-folding scale H~6 cm where the density with depth z is modeled as $\rho(z) = \rho_d - (\rho_d - \rho_s)e^{-z/H}$, where ρ_s is the density at the surface and ρ_d is the density at depth $z \gg H$. Mapping of variations in the modeled H parameter value by Hayne et al. (2017) showed local and regional differences in regolith properties where lower values of H indicate a regolith column with higher thermal inertia material closer to the surface and a higher H values indicate more insulating material near the surface. The model included a slope correction to account for the influence of topography on temperatures, and as a result, the H parameter mapping reveals the cold spots in greater detail than the regolith temperatures. For this reason, we additionally use this map to survey the largest population of cold spots with source craters $D \geq 800$ m.

The formation ages of the large craters were constrained using crater counts of the smaller crater populations superposed on their continuous ejecta. Counts were conducted using Arcmap with the Cratertools plugin (Kneissel et al., 2011)**.** LROC NAC images were calibrated and map-projected using ISIS (Integrated Software for Imagers and Spectrometers) with appropriate incidence angles for measuring crater diameters where optimal incidence angles are ~58° to ~77° (e.g., Antonenko et al., 2013; Ostrach et al., 2011). Because of the relatively young age of the ejecta, only craters with diameters generally no larger than a few tens of meters have had time to accumulate. The Neukum production function (NPF) (Neukum et al., 2001) only extends down to 10 m, and we therefore use the Williams et al. (2014) production function to derive model ages for the craters with the Craterstats2 program (Michael & Neukum, 2010) used to bin and fit to the crater size-frequency distributions (CSFDs). Williams et al. (2014) modeled lunar crater production down to a meter using the observed flux of objects colliding with the terrestrial atmosphere reported by Brown et al. (2002) and found model ages comparable to Neukum et al. (2001) with differences between the absolute model ages $<$15% for young surfaces.

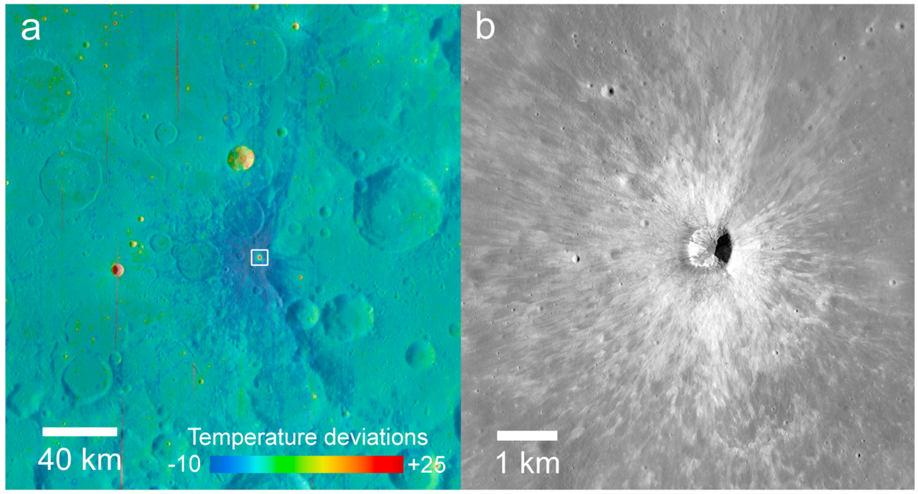

Figure 1. (a) Nighttime rock-free regolith temperature deviations (Bandfield et al., 2011) with LROC WAC global mosaic used for shading showing a cold spot associated with an ~0.9-km-diameter crater at 5.39°S, 90.76°E (labeled as crater number 5 in Figure 2 and Table 1). (b) Portion of LROC NAC image pair M1168926096 showing the cold spot source crater with the image location shown as a white box in (a).

3. Cold Spot Crater Population

Cold spot source craters have diameters ranging from 43 to 2,315 m (Figure 2). The CSFD of the total population (Figure 3) does not generally conform to the model Neukum production function (Neukum et al., 2001) with no single crater-age isochron describing the entire range of diameters. Diameters between 300 and 800 m are well approximated by an ~150-ka age isochron. Below *D*~300 m, the CSFD power law slope shallows with respect to the NPF and decreases substantially below *D*~100 m. Above *D*~800 m, craters are more numerous than predicted by a 150-ka isochron.

There is no indication that any of the cold spots result from secondary impacts. The source craters appear as fresh, isolated craters with no clustering or alignment and lack any of the morphologic features typically associated with secondary cratering such as shallow, irregular shapes, or asymmetric ejecta patterns in radial alignment with a primary source crater (McEwen & Bierhaus, 2006; Oberbeck & Morrison, 1973; Shoemaker, 1962).

The density of cold spots that have been identified diminishes with increasing latitude. The number of impacts is predicted to decline with latitude due to a higher probability of low inclination encounters, though this decline is estimated to result in only an ~10% difference in impact rate between the polar and equatorial regions (Gallant et al., 2009; Halliday, 1964; Ito & Malhotra, 2010; Le Feuvre & Wieczorek, 2008). The detection of cold spots becomes less reliable at higher latitudes due to the increasing topographic influence on surface temperatures, especially in the highlands. We therefore attribute the observed decline in cold spot density with latitude to a bias in observation. Absolute model ages have been derived from the CFSD for different latitude bands (Figure 4), demonstrating how the latitude bias influences derived model ages, which range from 220 ± 30 ka for latitudes 10°S to 10°N to 69 ± 10 ka for the highest latitudes 40° to 50°N/S. This can be further seen visually in Figure 2 at the higher latitudes of the survey where cold spots appear more numerous on the maria than the highlands, for example, the north portions of Oceanus Procellarum, and Mare Frigoris, Imbrium, and Serenitatis. Taking the craters at latitudes $>20°$ where the northern portions of these mare are located show the downturn in the CSFD at $D < 300$ m of the nearside is more modest than the farside due to a greater number of small cold spots identified at high latitudes in the maria relative to the highlands (Figure 5).

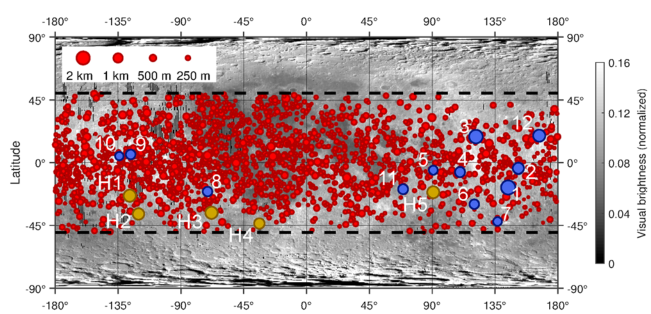

Figure 2. Locations of cold spot craters on Diviner map of visible surface brightness. Symbol sizes are scaled by crater diameter. Blue markers are the $D > 800$-m craters (labeled 1–12), and yellow symbols are the $D > 800$-m craters associated with cold spots that were identified in the *H* parameter map of Hayne et al. (2017) but were not apparent in the regolith temperature map (labeled H1–H5).

10.1029/2018JE005652

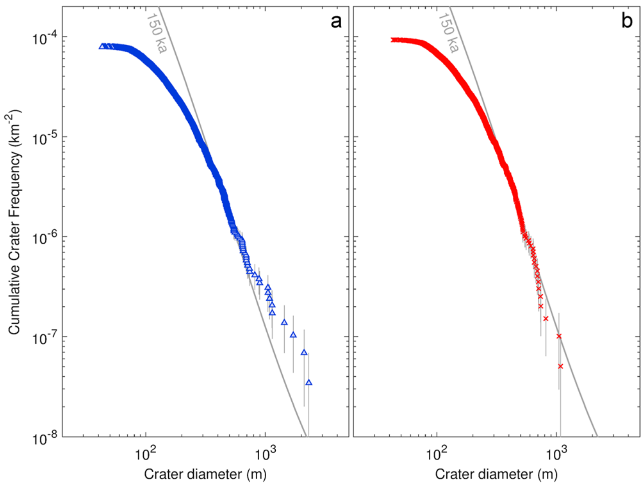

Figure 3. (a) The CSFD of the survey of source craters of cold spots identified in the regolith temperature map of Bandfield et al. (2011). (b) The CSFD of the survey excluding longitudes 65°E–180°E where the majority of large cold spots occur. The gray curve is the Neukum production function (Neukum et al., 2001) for a 150-ka age surface.

This suggests that the greater topographic variability of the highlands makes detection of smaller cold spots more difficult at higher latitudes relative to the maria and further suggest that the downturn in the CSFD is a result of incomplete cold spot detection at smaller sizes.

Additional heterogeneities are observed in the distribution of cold spots. In addition to the variation with latitude discussed above, the density of cold spots varies with longitude (Figure 6) with a maximum around 90°W and a minimum around 90°E. These longitudes correspond to the centers of the leading and trailing hemispheres, respectively (apex and antapex of motion) for the synchronously rotating Moon. The cold spot density declines with angular distance from the apex and the relative change in density is approximated by a best fit sinusoid $[1 + 0.125\cos(\beta)]^{2.74}$, a relationship derived by Zahnle et al. (2001) for a synchronous moon in an isotropic impactor population where β is the angular distance from the apex.

The largest cold spot craters, however, do not follow this trend, but instead show a higher abundance of craters $D > 800$ m on the farside of the trailing hemisphere. The survey of cold spots found 12 source craters $D > 800$ m with all but three occurring between 65°E and 180°E (labeled *1–12* in Figure 2). An equatorial survey (±10° latitude) of cold spots by Powell et al. (2018), using the *H* parameter map of Hayne et al. (2017), found a greater number of cold spots than identified by regolith nighttime temperatures alone. Cold spots with more subtle temperature contrasts are more apparent in the *H* parameter map (Powell et al., 2018) in part, because the *H* parameter map has the influence of slopes modeled out, and as a result, cold spots stand out against the background more clearly, especially at higher latitudes. We therefore additionally surveyed the *H* parameter map between ±50° latitude for all cold spots with source craters $D \geq 800$ m. This revealed an additional five cold spots that are not identifiable in nighttime regolith temperatures. The temperature anomalies of these craters are small, all with a temperature contrast of less than 2.5 K from the background; however, cold slopes in the surrounding areas vary ~4–10 K, and therefore, these cold spots are only apparent in the *H* parameter map. These craters are denoted in Figure 2 by yellow markers and labeled *H1–H5*.

The cold spot CSFD overlaps the NPF for surface ages of several hundred ka (Figures 3 and 4), providing an estimate of the length of time cold spots endure. The crater counts on the ejecta of the largest cold spot source craters ($D > 800$ m) further constrain the ages of cold spots. Counts were conducted on the ejecta on all but two craters (numbered 8 and 10 in Figure 2) as these craters occur on the inner walls of larger craters where slopes are high and crater counts could not be reliably conducted. The absolute model ages are

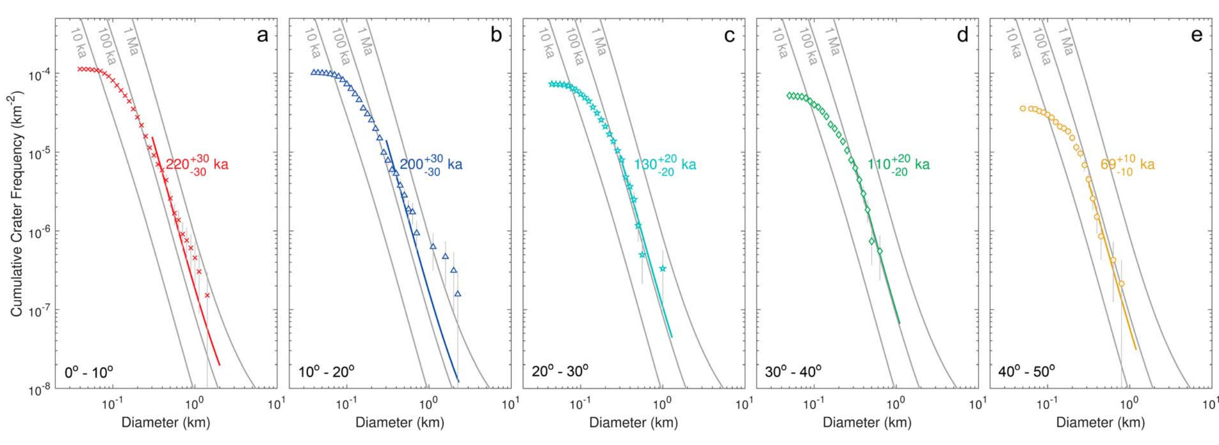

Figure 4. The CSFD of cold spot craters for latitudes. (a) 0°–10°N/S. (b) 10°–20°N/S. (c) 20°–30°N/S. (d) 30°–40°N/S. (e) 40°–50°N/S. The model ages for craters $D > 300$ m for each latitude range (color curves) and 10-ka, 100-ka, and 1-Ma model age isochrons (gray curves) using the NPF are shown.

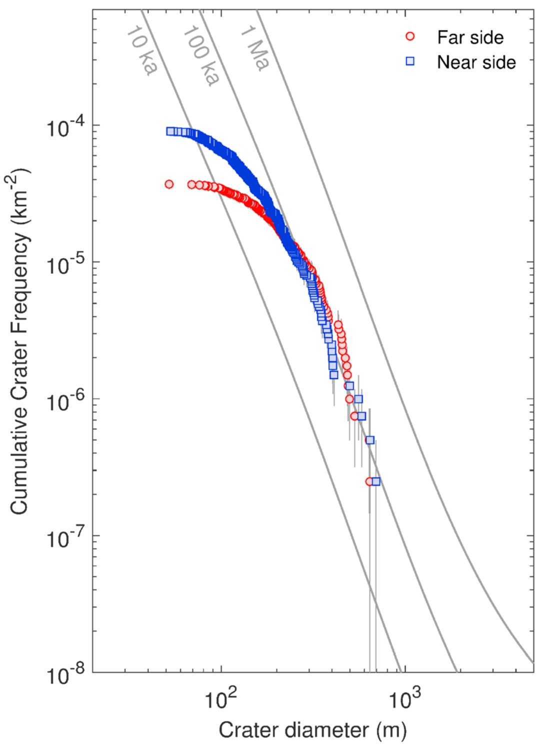

Figure 5. The CSFDs of cold spot craters for latitudes >20°N split into nearside and farside populations.

summarized in Table 1 and Figures 7 and S1 and vary between 220 ka and 1.3 Ma. Seven of the 10 large cold spots identified in the nighttime regolith temperature map are younger than 500 ka. The five cold spots that were not apparent in the regolith temperature map, but were identified using the *H* parameter map, are all older than 500 ka. Evidence of self-secondary cratering has been noted (Williams, van der Bogert, et al., 2018; Zanetti et al., 2017) and we were careful to avoid areas where craters were clustered and/or appeared as part of a boulder track, that is, a linear distribution of craters, often elliptical, aligned downslope. The inclusion of unknown self-secondaries would increase the apparent age, and as such, these ages would represent an upper limit.

4. Discussion

4.1. Cold Spot CSFD

Cosmic-ray exposure ages of Apollo 16 samples constrain the age of South Ray crater (D = 680 m) to 2 ± 0.2 Ma (Drozd et al., 1974; Eugster, 1999; Stöffler & Ryder, 2001). South Ray crater does not have a definitive cold spot associated with it, providing evidence that cold spots do not survive beyond this age and are relatively ephemeral features on the lunar surface. Applying the idealized crater retention age to the cold spot source crater distribution provides an estimate of the typical retention time of the cold spots detectible in the regolith nighttime temperature data. Diameters between 300 and 800 m are well approximated by a 150-ka isochron, though, as noted in section 3, using only the craters within ±10° of the equator where the observations are not biased by latitude, and therefore, cold spot detection is likely more robust, are better fit by a 220-ka isochron (Figure 4). Deviations between the measured distribution and the model distributions could indicate variations in retention times for differing cold spot sizes. Additionally, the shallower CSFD slope observed at smaller diameters may result from the incomplete identification of cold spots at smaller sizes as the ability to discern cold spots from slope effects and other temperature heterogeneities becomes more difficult as noted above, or there may be additional factors in cold spot formation at smaller impact energies that influence the expression of cold spots and the magnitude of the associated thermal anomalies (i.e., a lower limit to cold spot formation). The apparent increase in crater abundance above that predicted by the NPF for diameters above ~800 m results from a population of larger craters in the eastern hemisphere farside (Figure 2). The CSFD of the cold spot craters excluding longitudes 65°E–180°E are better approximated by a single isochron for all diameters ≳300 m (Figure 3b).

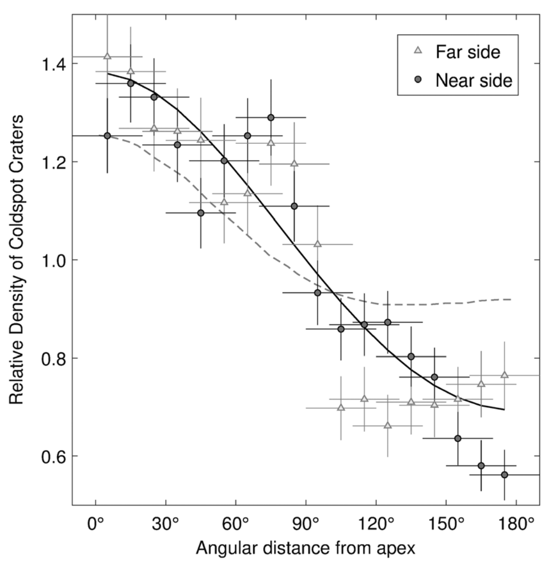

Figure 6. Distribution of the relative cold spot crater density as a function of angular distance from the apex of lunar orbital motion for the nearside (circles) and farside (triangles). The density of craters averaged over an angular distance of 30° is plotted every 10°. Solid curve is a least squares fit sinusoid $[1 + 0.125\cos(\beta)]^{2.74}$ And dashed gray curve is the predicted relative cratering rate for crater diameters larger than 1 km of Le Feuvre and Wieczorek (2011) for the entire moon.

New impacts that have formed during the lifetime of the LRO mission have been detected by LROC NAC temporal ("before and after") image pairs (Speyerer et al., 2016). The number of new craters with diameters ≥10 m is modestly higher (33%) than the rate of crater production predicted by the NPF, but well within the uncertainty often ascribed to the crater age-dating technique (see recent papers by Fassett, 2016; Hartmann & Daubar, 2017; Williams, van der Bogert, et al., 2018, and references therein). Broad zones of reflectance changes associated with the fresh craters may be related to surface-bound jetting processes and extend from their source craters at a similar scale to cold spots observed at larger sizes resolvable by the Diviner instrument. It is important to note that these reflectance changes are only visible in "phase ratio" images formed by comparing before and after images with specific geometry; therefore, the reflectance changes associated with these extended zones are not

Table 1
Summary of D > 800-m Cold Spot Source Craters (See Figure 2 for Map Locations) With Absolute Model Ages (AMAs) From Williams et al. (2014)

Crater no.	Longitude	Latitude	Diameter (m)	Model age (ka)
1	144.40	−17.68	2315	990 ± 40
2	151.68	−4.08	1442	220 ± 10
3	121.31	18.68	2112	420 ± 70
4	109.91	−6.74	1143	480 ± 30
5	90.76	−5.39	898	230 ± 20
6	120.12	−29.73	1051	380 ± 40
7	136.80	−42.16	886	770 ± 60
8	−70.92	−20.62	1053	-
9	−126.00	5.82	1085	420 ± 70
10	−134.10	4.60	816	-
11	69.14	−18.92	1140	270 ± 20
12	166.64	19.38	1714	1100 ± 100
H1	−126.64	−23.60	1739	810 ± 80
H2	−120.37	−36.75	1538	1200 ± 50
H3	−68.07	−35.89	1750	590 ± 40
H4	−33.81	−43.62	1277	620 ± 40
H5	80.73	−21.09	1670	1300 ± 200

generally identifiable for small craters without preimpact imagery. If these zones of modified reflectance are related to cold spots, then it implies that cold spot production does in fact extend to smaller size craters at a rate more consistent with NPF and the down turn in the cold spot CSFD at smaller diameters is due to more rapid fading of small cold spots or the reliability of cold spot detection by Diviner diminishing below diameters ~300 m (or both).

The smallest cold spot in the survey has a diameter of 43 m. Several of the largest new craters identified by LROC NAC temporal pairs, diameters 73, 50, and 43 m, with before and after Diviner coverage show the appearance of cold spots associated with the formation of these craters (Figure 8). Several smaller new craters with diameters 35, 34, and 30 m, also with before and after Diviner coverage, did not have identifiable cold spots, providing an indication that cold spot detection by Diviner is limited to craters above these sizes. Impact craters generated by the Ranger spacecraft and the Apollo S-IVB boosters have been identified in LROC NAC images, and formed ~15- and ~35-m craters, respectively (Plescia et al., 2016; Wagner et al., 2017). These did not generate identifiable cold spots. As additional postimpact data are acquired, further analyses of new cold spots may enable a better understanding of the temporal evolution of the smallest cold spots.

4.2. Spatial Distribution

Impacts are expected to preferentially impact on the leading hemisphere of a synchronously rotating satellite with the highest rate of impacts occurring at the apex of motion at 90°W and the frequency of impacts dropping with longitude toward the center of the trailing hemisphere at 90°E (Gallant et al., 2009; Horedt & Neukum, 1984; Ito & Malhotra, 2010; Le Feuvre & Wieczorek, 2011; Morota & Furumoto, 2003; Morota et al., 2005, 2008; Shoemaker & Wolfe, 1982; Wood, 1973; Zahnle et al., 1998, 2001). The magnitude of the asymmetry will depend on the orbital velocity of the satellite relative to the mean impactor encounter velocity, and therefore, the leading/trailing asymmetry in the distribution of cold spots has potential implications for the dynamical origins of the small D = 1–100-m projectiles that created them. If the relative velocities between the impactors and the Moon-Earth system are similar, the cratering asymmetry will be more pronounced. The ratio of cold spot craters between the apex and antapex of motion is nearly 2 (Figure 6). This precludes an impactor source population predominately composed of objects with high encounter velocities such as comets (Hughes & Williams, 2000).

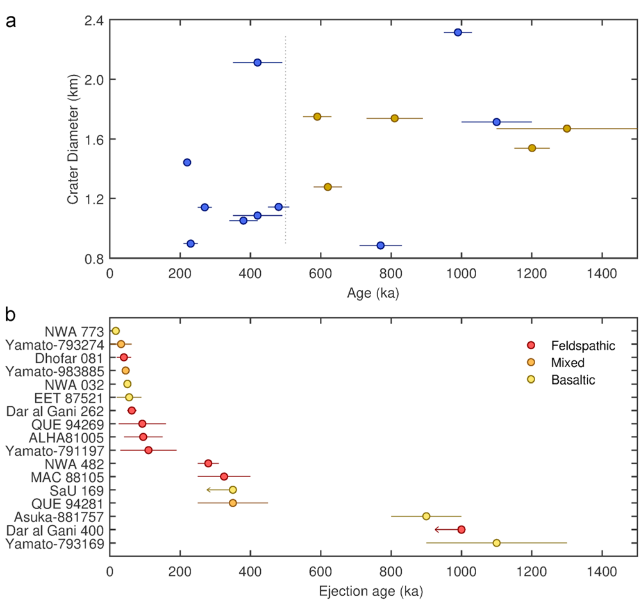

Figure 7. (a) The absolute model ages derived from crater counts on the ejecta of the large (D > 800 m) cold spot craters where *blue* markers are cold spots observed in regolith nighttime temperatures and *yellow* markers are cold spots only observed in H parameter maps as in Figure 2 (see also Table 1). Error bars are statistical uncertainties in crater counts. Vertical dashed line denotes 0.5-Ma age. (b) Selection of lunar meteorites with available ejection ages between 0 and 1.4 Ma (for references, see Lorenzetti et al., 2005).

A survey of rayed craters using Clementine 750-nm mosaic images with diameters 5 km and larger found an apex-antapex ratio of ~1.65 with smaller ratios for larger craters (Morota & Furumoto, 2003). Morota et al. (2005), using the approximate analytic cratering asymmetry estimate of Zahnle et al. (2001), inferred impact velocities to be 12–16 km/s from this asymmetry. The larger leading-trailing asymmetry we observe in the cold spots is similar to the asymmetry identified in the spatial distribution of impact sites determined by Apollo seismic data (1.8 ± 0.5) (Morota et al., 2011), implying even lower average impact velocities of ~8–9 km/s. However, estimates of mean Earth-Moon encounter velocities are higher. Dynamical modeling of near-Earth asteroids predicts impact velocities ~19–22 km/s, which results in more modest predicted leading/trailing ratios of ~1.3 (Gallant et al., 2009; Ito & Malhotra, 2010; Le Feuvre & Wieczorek, 2011). A more extensive search for rayed craters down to

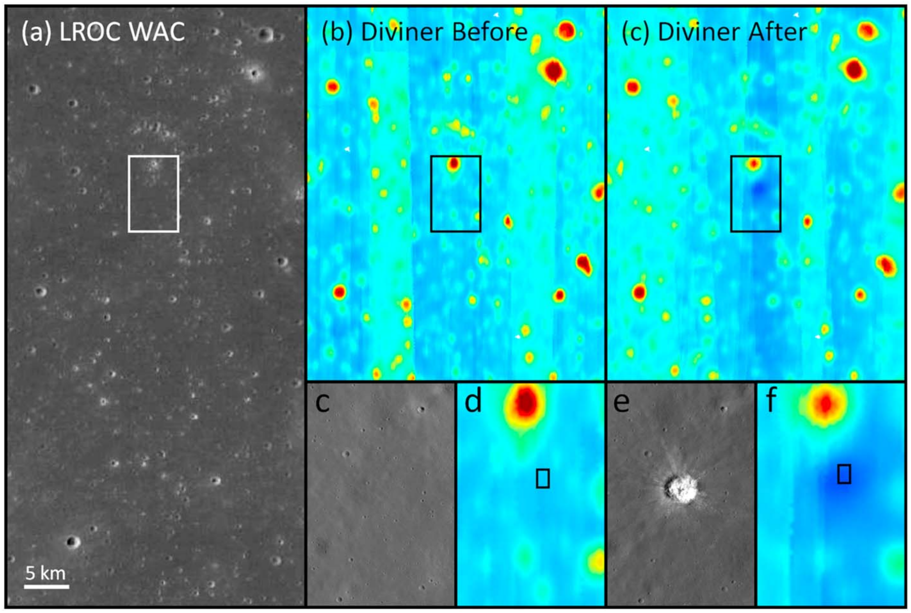

Figure 8. Diviner temperature data collected before and after some new impacts show the creation of new cold spots. (a) LROC WAC image of central Mare Humorium and (b) Diviner Ch 8 (50–100 μm) nighttime brightness temperature data collected before and (c) after the formation of an ~70-m crater identified using LROC temporal pair NAC imagery (Speyerer et al., 2016). Boxes show locations of subframes (d) and (f) highlighting the new ~2.8-km cold spot. Boxes in (d) and (f) are location of subframes (c) and (e) showing a portion of (c) LROC NAC image m114213813 acquired on 30 November 2009 and (d) image m1249810950 acquired on 5 May 2017 before and after the crater formed, respectively.

diameters as small as 500 m found the spatial distribution of rayed crater densities correlate with model-predicted distributions when hemispherically averaged. However, averaging over a 30° window reveals a patchy distribution of crater densities that do not conform well to model predictions, including higher crater densities at high latitudes, contradicting expectations (Werner & Medvedev, 2010).

The slower than predicted impact velocities of <12 km/s implied by the asymmetry of the lunar rayed craters reported by Morota and Furumoto (2003), led Ito and Malhotra (2010) to speculate that an unobserved slower than average population of objects with heliocentric orbits close to the Earth-Moon system may exist. The asymmetry of the cold spots supports the existence of a population of low-velocity objects with mean velocities relative to the Earth of only v_∞~5–6 km/s, accounting for the acceleration due to gravity of the Earth-Moon system assuming an escape velocity

$$v_{\mathrm{esc}} = \sqrt{2G\left(\frac{M_{\mathrm{Earth}}}{D_{\mathrm{Moon}}} + \frac{M_{\mathrm{Moon}}}{R_{\mathrm{Moon}}}\right)} \tag{1}$$

where G is the gravitational constant; M_{Earth} and M_{Moon} are the masses of the Earth and Moon, respectively; D_{Moon} is the lunar distance from Earth; and R_{Moon} is the radius of the Moon. Such slow objects would be nearly co-orbiting the Earth, making them potential candidates for in situ resource utilization and suitable targets for NASA's Asteroid Redirect Mission (ARM) as objects for such missions need to be accessible with low Δv (Abell et al., 2009; Binzel et al., 2004; Mainzer et al., 2011; Schunová-Lilly et al., 2017).

The mean collision lifetime of low encounter velocity asteroids in near-Earth orbits is short. Objects just able to get from Venus or Mars have a collisional lifetime of only about a million years with shorter time scales for slower objects (Harris & D'Abramo, 2015). Additionally, numerous secular perturbations and resonances in the orbital zones of the terrestrial planets can pump up the velocities of small bodies (Michel & Froeschlé, 1997). Such slow objects would therefore need to be continuously resupplied. A tidal disruption event of a larger low-v_∞ asteroid during a close encounter with Earth could have increased the population of smaller objects in Earth-like orbits and contributed to the asymmetry of cold spot formation. These objects tend to return to reimpact the Earth and Moon, causing a spike in the impact rate within 10^5 years following the

10.1029/2018JE005652

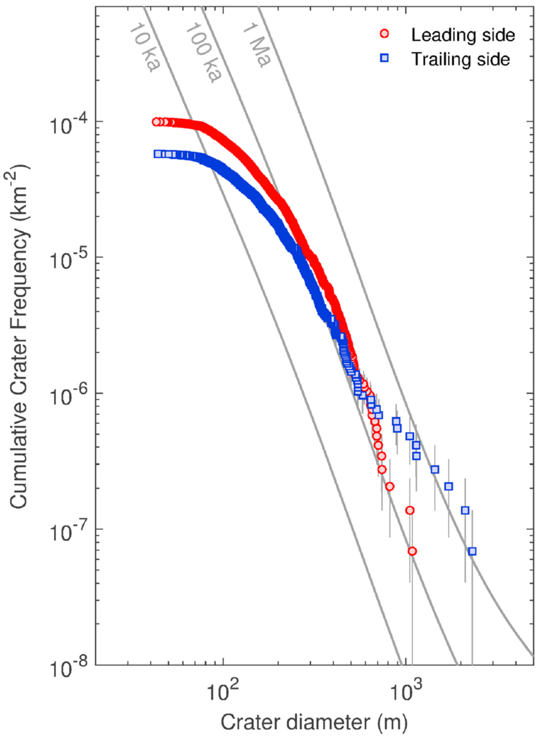

Figure 9. The CSFD of the cold spot source craters for the leading (western) hemisphere and trailing (eastern) hemisphere. The difference between the hemispheres increases with decreasing crater diameter.

disruption event (Schunová et al., 2014). Alternately, impacts on the Moon could provide a population of low-v_∞ near-Earth asteroids. The lunar meteorites provide evidence for the viability of lunar impact ejecta as such a source. Studies of the dynamical evolution of lunar fragments ejected from the Moon find a fraction of the fragments that escape the Earth-Moon system into heliocentric orbits return to reimpact in tens of thousands of years (Gladman et al., 1995). These scenarios could also explain a size dependence we observe in the leading/trailing asymmetry (Figure 9) as the mass of low-v_∞ material would be distributed as smaller collisional debris.

The distribution of large cold spots does not follow the trend in leading-trailing asymmetry of crater densities. While the size-frequency distribution of the cold spot craters is consistent with a crater-age isochron ~100–200 ka, the power law slope of the CSFD at diameters larger than 800 m is shallower, with the largest craters overlapping the ~1-Ma isochron (Figures 3 and 9). This apparent excess of larger craters relative to the smaller craters is attributed to a concentration of large craters occurring on the trailing hemisphere that are generally clustered on the lunar farside, centered near 130°E longitude (Figure 2). Williams, Bandfield, et al. (2017) suggested that this distribution could have resulted from a swarm of fragments impacting the trailing farside in a single event.

To test the significance of the distribution of this population of craters, we apply the Rayleigh z test to the distribution of longitudes (i.e., test the probability of randomness in an angular distribution around a circle) (Batschelet, 1981; Mahan, 1991; Zar, 1984). The basic principle is to define a vector $\overline{R}$ that indicates one sidedness, or how concentrated versus dispersed the data are around a circle, where $\overline{R} = \sqrt{X^2 + Y^2}$ is the mean resultant vector length and $Y = \frac{1}{n}\sum_{i=1}^{n} \sin\varphi_i$ and $X = \frac{1}{n}\sum_{i=1}^{n} \cos\varphi_i$ are the rectilinear coordinates of the mean where φ_i are the angular values and n is the sample size. A uniform distribution has a value of $\overline{R} = 0$ and a value of 1 for complete concentration in one direction; thus, if $\overline{R}$ is sufficiently large, then randomness can be rejected in favor of a single preferred direction. If the Rayleigh Z-statistic, $Z = n\overline{R}^2$, is larger than a critical Z value, then there is strong evidence against the null hypothesis of no sample mean direction. Taking the 12 large $D > 800$-m craters observed as cold spots in the regolith temperatures, we calculate $Z = 3.7935$ which corresponds to a p value of 0.019, that is, the probability of finding the observed result when the null hypothesis is true. The critical Z, typically defined by a p value of 0.05, is 2.932 for $n = 12$ (Zar, 1984). As we exceed this value, we can conclude that the null hypothesis of no preferred longitude can be rejected with high confidence. This would be a conservative estimate as it assumes equal probability of craters forming at any longitude; however, the leading hemisphere is favored due to the synchronous rotation.

Our survey of the H parameter map revealed five additional large cold spots, four of which occur in the leading hemisphere (Williams, Bandfield, et al., 2018). Crater counts conducted on the continuous ejecta of the large cold spot craters also yield a range of absolute model ages (~200–1300 ka) (Figure 7). The cold spots apparent only in the H parameter map are all older than 0.5 Ma. The other cold spots are generally younger than 0.5 Ma, with the exception of three which are older and the two that could not be dated (craters 8 and 10 in Figure 2). This indicates that cold spots cannot be reliably detected by regolith temperatures alone after ~0.5 Ma, but can persist to ages older than ~1 Ma. The ages also suggest that cold spots of the larger craters have a longer lifetime than implied by the overall CSFD, which largely overlaps an ~100–200-ka isochron.

The distribution of the older cold spots (>0.5 Ma) is more consistent with a random distribution, and the variations in ages for the younger craters (0.2–0.5 Ma) show they are not related to a single event as proposed by Williams, Bandfield, et al. (2017). However, as seen with the smaller craters, the large cold spots should form preferentially in the leading hemisphere, which is not observed. Twice as many large young craters

(<0.5 Ma) occur on the trailing side as on the leading side and several have overlapping model ages. Therefore, a multiimpact event from a small binary or triple near-Earth asteroid (e.g., Margot et al., 2015) on the trailing farside forming several near-simultaneous craters within the last 0.5 Ma cannot be ruled out as a possible explanation for the distribution of the large cold spots.

Alternatively, the destruction rate of the large cold spots could be enhanced on the leading hemisphere. The formation and destruction of cold spots is not well understood, making this scenario difficult to assess. Smaller impacts, down to the limit of Diviner spatial resolution, also appear to create cold spots, and it is not clear how their destruction results from the superposition of additional impacts. A comparison of the CSFD of the cold spot craters on the leading and trailing hemispheres shows that the leading-trailing asymmetry is largest for the smallest cold spots (Figure 9). This could result from slower mean impact velocities for the smaller impactors, consistent with the asymmetry observed in impact events detected by the Apollo Passive Seismic Experiment which represent craters 1–50 m in diameter (Morota et al., 2011; Oberst et al., 2012). The velocity distribution for impactors forming the meter-scale craters may therefore differ from those forming the kilometer-scale craters. If true, the leading-trailing asymmetry will be size dependent and could result in a more rapid destruction of larger cold spots on the leading hemisphere and explain why the CSFDs of the leading and trailing hemispheres cross over at diameters ~800 m. Further, Powell et al. (2018) find evidence that cold spots initially degrade rapidly, with degradation rates slowing as they become more faint, and thus, the younger large cold spots would be most sensitive to an asymmetric degradation rate, explaining why the younger, <0.5 Ma, large cold spots are concentrated on the trailing side. Similarly, the contradicting observation of a higher frequency of bright-rayed craters at high latitudes by Werner and Medvedev (2010) could result from enhanced micrometeorite bombardment at equatorial latitudes, which accelerates the maturation of the ray materials. Since cold spots are more difficult to detect at higher latitudes, we are unable to explore any latitude dependence on cold spots with any confidence.

4.3. Source of Lunar Meteorites

Lunar meteorites represent fragments of the lunar near-surface crust ejected from the Moon by meteoroid impacts. The precise provenance on the lunar surface of the meteorites is unknown and they likely represent a sampling from both the nearside and farside. Meteorites for which cosmic-ray exposure data are available show that all of the meteorites were launched from the Moon within the last 20 Myr, with most being ejected in the last 0.5 Myr (Eugster et al., 2006; Korotev, 2005; Lorenzetti et al., 2005) (Figure 7). Because of the diversity of compositions and exposure ages, the meteorites likely derive from many craters, and the young ejection ages constrain the source craters to less than a few kilometers in diameter as there are not enough larger craters young enough to account for the diversity of meteorites (Basilevsky et al., 2010; Warren, 1994). Therefore, many of the known lunar meteorites likely originated from craters with cold spots.

Hydrocode simulations find impact events forming craters with diameters as small 1.1 km can produce enough sizable fragments with lunar escape velocities (2.38 km/s) to account for the largest meteorite samples (Head, 2001). No cold spot craters larger than 800 m were found in the maria; thus, the basaltic meteorites sourced from mare with ejection ages of less than a few hundred kyr must have been launched by impacts forming craters smaller than 800 m. This is supported by generally shallow, less than a few meters, meteorite source depths and a large fraction of the meteorites being composed of regolith breccias formed within the regolith layer (Basilevsky et al., 2010; Lorenzetti et al., 2005). Therefore, cold spot craters larger than several hundred meters are candidate source craters for the meteorites and the ejection ages of many of the meteorites overlap with the formation ages of the largest cold spots (Figure 7).

We note that the proposed D ~1.4-km source crater on the floor of Schickard crater for the meteorites Yamato-793169, Asuka-881757, MIL 05035, and MET 01210, which are suggested to be launch paired (Arai et al., 2010), does not have an identifiable cold spot in either the regolith temperatures or H parameter. However, the CRE ages, indicating launch ages around 1 Ma, would be approximately consistent with the age of the oldest cold spots we have been able to identify, and thus, it is possible that this crater formed a cold spot that is no longer detectable.

4.4. Impact Gardening Rates

The persistence of cold spot thermal signatures throughout the lunar night implies that the layer of modified regolith extends to a depth at least 5 cm and possibly several tens of centimeters for the most prominent cold spot surfaces (Bandfield et al., 2014; Hayne et al., 2017). How cold spots are removed is not clear; however, the preservation time scale for the cold spots suggests that cold spots are reworked into background regolith to these depths over ~10^5–10^6 years.

Analytic modeling of regolith overturn and mixing rates generated by the present-day impact flux (e.g., Brown et al., 2002) predict a depth of regolith overturn with time that is slower by several orders of magnitude than implied by the cold spots (Costello et al., 2017; Gault et al., 1974; Lucey et al., 2018). Costello et al. (2018) found that the present-day population of impactors only overturns the regolith to a depth of a couple millimeter in 5 Myr. Studies of Apollo drill cores however find that vertical mixing of nanophase FeO, cosmic-ray tracks, cosmogenic radionuclides, and other products of regolith maturation that accumulate at the surface (e.g., Blanford, 1980; Fruchter et al., 1977; Morris, 1978) require much higher overturn rates. Secondary craters, craters formed by fragments ejected by the original primary impact event, have been suggested to form a substantial fraction of the total population of craters (e.g., Bierhaus et al., 2018; McEwen et al., 2005; Shoemaker, 1965; Williams, 2018), and Costello et al. (2018) find that estimates of regolith overturn-depth rates that include secondary cratering are in good agreement with the analysis of the Apollo cores. This model estimates that in 300 kyr, there is a 99% chance of the regolith being overturned one or more times to a depth of ~12 cm and a 99% chance of the regolith being overturned 100 or more times at a depth of 5 cm, which is broadly consistent with our estimates of the cold spot lifetimes of less than ~1 Myr (i.e., 5 cm to $>$10 cm overturned in a few hundred kiloyear). Further, this is also consistent with the formation rate of "splotches," reflectance changes associated with the new craters formed during the LRO mission (Speyerer et al., 2016). These features, identified by LROC NAC temporal image pairs, indicate that the top 2–3 cm of regolith are modified on a time scale of ~80,000 years. This collectively suggests that secondary cratering is the predominant mechanism of mixing of the top meter of the lunar regolith.

5. Conclusions

Cold spots last a few 100 ka as estimated from fitting the NPF to the cold spot source craters' size-frequency distribution. Larger cold spots may persist longer as they are in greater abundance than predicted given the CSFD at smaller crater diameters, and crater counts on the ejecta of the largest craters ($D > 0.8$ km) yield absolute model ages that range from ~200 ka to ~1.1 Ma. Five large cold spots, not identifiable in the regolith temperatures, but apparent in the H parameter map, are all older than 0.5 Ma, indicating that weak, faded cold spots can persist for $>$0.5 Ma but are not reliably detected by temperatures alone. The survival time of these features requires a relatively rapid regolith overturn rate consistent with secondary cratering playing a predominate role.

An asymmetry in the distribution of the cold spots reflects the synchronous rotation of the Moon, with a larger number of cold spots occurring on the leading hemisphere. The ratio of the crater density at the apex of motion versus the antapex of motion is nearly 2, requiring the impactor population forming these craters to be slower on average than typically predicted and slower than estimated for the rayed craters. The leading-trailing asymmetry is greatest for the smaller diameter craters and the trend is inverted for craters larger than ~800 m, with a greater density of craters in the trailing hemisphere. This could mean that the distribution of encounter velocities is lower for smaller impactors and could result from a population of small, meters-to-tens of meters, slow objects in heliocentric orbits close to the Earth-Moon system. Additionally, the higher rate of smaller impacts on the leading hemisphere could contribute to the destruction of cold spots, resulting in a more rapid fading of larger cold spots on the leading side. Deviations in the rayed crater distribution from an idealized production function have similarly been suggested to indicate a size-dependent retention time (Werner & Medvedev, 2010). Alternatively, a multiimpact event from a swarm of ~100-m-scale meteoroids impacting on the trailing farside in the last 0.5 Myr could explain the overabundance of larger cold spots in this part of the Moon.

Acknowledgments
We would like to thank two anonymous reviewers for their helpful comments and Jaahnavee Venkatraman for the helpful edits. We also would like to thank the LRO, LROC, and Diviner operations teams for the collection of the high-quality data sets used in this work. The data used in this study are publicly available via the Geosciences Node of the Planetary Data System (http://pdsgeosciences.wustl.edu/missions/lro/diviner.htm) and the LROC Data Node (http://lroc.sese.asu.edu/). The contributions of J.-P. Williams were funded by a NASA Solar System Workings grant 80NSSC18K0010. Part of this work was supported by the NASA Lunar Reconnaissance Orbiter project.

References

Abell, P. A., Korsmeyer, D. J., Landis, R. R., Jones, T. D., Adamo, D. R., Morrison, D. D., et al. (2009). Scientific exploration of near-Earth objects via the Orion Crew exploration vehicle. *Meteoritics and Planetary Science*, *44*(12), 1825–1836. https://doi.org/10.1111/j.1945-5100.2009.tb01991.x

Antonenko I., Robbins S. J., Gay P. L., Lehan C., & Moore J. (2013). Effects of incidence angle on crater detection and the lunar isochron system: Preliminary results from the Cosmoquest Moonmappers citizen science project. *Lunar and Planetary Science Conference*, *44th*, abstract #2705.

Arai, T., Hawke, B. R., Giguere, T. A., Misawa, K., Miyamoto, M., & Kojima, H. (2010). Antarctic lunar meteorites Yamato-793169, Asuka-881757, MIL 05035, and MET 01210 (YAMM): Launch pairing and possible cryptomare origin. *Geochimica et Cosmochimica Acta*, *74*(7), 2231–2248. https://doi.org/10.1016/j.gca.2009.11.019

Bandfield, J. L., Ghent, R. R., Vasavada, A. R., Paige, D. A., Lawrence, S. J., & Robinson, M. S. (2011). Lunar surface rock abundance and regolith fines temperatures derived from LRO Diviner radiometer data. *Journal of Geophysical Research*, *116*, E00H02. https://doi.org/10.1029/2011JE003866

Bandfield, J. L., Song, E., Hayne, P. O., Brand, B. D., Ghent, R. R., Vasavada, A. R., & Paige, D. A. (2014). Lunar cold spots: Granular flow features and extensive insulating materials surrounding young craters. *Icarus*, *231*, 221–231. https://doi.org/10.1016/j.icarus.2013.12.017

Basilevsky, A. T., Neukum, G., & Nyquist, L. (2010). The spatial and temporal distribution of lunar mare basalts as deduced from analysis of data for lunar meteorites. *Planetary and Space Science*, *58*(14-15), 1900–1905. https://doi.org/10.1016/j.pss.2010.08.020

Batschelet, E. (1981). *Circular Statistics in Biology*. New York, NY: Academic Press.

Bierhaus, E. B., McEwen, A. S., Robbins, S. J., Singer, K. N., Dones, L., Kirchoff, M. R., & Williams, J.-P. (2018). Secondary craters and ejecta across the solar system: Populations and effects on impact-crater based chronologies. *Meteoritics & Planetary Science*, *53*(4), 638–671. https://doi.org/10.1111/maps.13057

Binzel, R. P., Perozzi, E., Rivkin, A. S., Rossi, A., Harris, A. W., Bus, S. J., et al. (2004). Dynamical and compositional assessment of near-Earth object mission targets. *Meteoritics and Planetary Science*, *39*(3), 351–366. https://doi.org/10.1111/j.1945-5100.2004.tb00098.x

Blanford, G. (1980). Cosmic ray production curves below reworking zones. *Lunar and Planetary Science Conference Proceedings*, *11*, 1357–1368.

Brown, P., Spalding, R. E., ReVelle, D. O., Tagliaferri, E., & Worden, S. P. (2002). The flux of small near-Earth objects colliding with the Earth. *Nature*, *420*, 294–296. https://doi.org/10.1038/nature01238

Costello, E. S., Ghent, R. R., & Lucey, P. G. (2017). A refreshed model for the mixing rate of lunar regolith. *Lunar and Planetary Science Conference*, *48th*, abstract #1672.

Costello, E. S., Ghent, R. R., & Lucey, P. G. (2018). The mixing of lunar regolith: Vital update to a canonical model. *Icarus*, *314*, 327–344. https://doi.org/10.1016/j.icarus.2018.05.023

Drozd, R. J., Hohenberg, C. M., Morgan, C. J., & Ralston, C. E. (1974). Cosmic-ray exposure history at the Apollo 16 and other lunar sites: Lunar surface dynamics. *Geochimica et Cosmochimica Acta*, *38*(10), 1625–1642. https://doi.org/10.1016/0016-7037(74)90178-1

Eugster, O. (1999). Chronology of dimict breccias and the age of south ray crater at the Apollo 16 site. *Meteoritics and Planetary Science*, *34*(3), 385–391. https://doi.org/10.1111/j.1945-5100.1999.tb01347.x

Eugster, O., Herzog, G. F., Marti, K., & Caffee, M. W. (2006). Irradiation records, cosmic-ray exposure ages, and transfer times of meteorites. In D. S. Lauretta, & H. Y. McSween (Eds.), *Meteorites and the Early Solar System II*, (pp. 829–851). Tucson, AZ: Univ. of Arizona Press.

Fassett, C. I. (2016). Analysis of impact crater populations and the geochronology of planetary surfaces in the inner solar system. *Journal of Geophysical Research: Planets*, *121*, 1900–1926. https://doi.org/10.1002/2016JE005094

Fruchter, J., Rancitelli, L., Laul, J., & Perkins, R. (1977). Lunar regolith dynamics (Pembroke, Ont.) based on analysis of the cosmogenic radionuclides ^{22}Na, ^{26}Al, and ^{53}Mn. *Lunar and Planetary Science Conference Proceedings*, *8*, 3595–3605.

Gallant, J., Gladman, B., & Ćuk, M. (2009). Current bombardment of the earth-moon system: Emphasis on cratering asymmetries. *Icarus*, *202*(2), 371–382. https://doi.org/10.1016/j.icarus.2009.03.025

Gault, D. E., Hörz, F., Brownlee, D. E., & Hartung, J. B. (1974). Mixing of the lunar regolith. *In Lunar and Planetary Science Conference Proceedings*, *5*, 2365–2386.

Gladman, B. J., Burns, J. A., Duncan, M. J., & Levinson, H. F. (1995). The dynamical evolution of lunar impact ejecta. *Icarus*, *118*(2), 302–321. https://doi.org/10.1006/icar.1995.1193

Halliday, I. (1964). The variation in the frequency of meteorite impact with geographic latitude. *Meteoritics*, *2*(3), 271–278. https://doi.org/10.1111/j.1945-5100.1964.tb01433.x

Harris, A. W., & D'Abramo, G. (2015). The population of near-Earth asteroids. *Icarus*, *257*, 302–312. https://doi.org/10.1016/j.icarus.2015.05.0040019-1035

Hartmann, W. K., & Daubar, I. J. (2017). Martian cratering 11. Utilizing decameter scale crater populations to study Martian history. *Meteoritics and Planetary Science*, *52*(3), 493–510. https://doi.org/10.1111/maps.12807

Hayne, P. O., Bandfield, J. L., Siegler, M. A., Vasavada, A. R., Ghent, R. R., Williams, J. P., et al. (2017). Global regolith thermophysical properties of the moon from the Diviner Lunar Radiometer Experiment. *Journal of Geophysical Research*, *122*, 2371–2400. https://doi.org/10.1002/2017JE005387

Head, J. N. (2001). Lunar meteorite source crater size: Constraints from impact simulations. *Lunar and Planetary Science Conference*, *32nd*, abstract #1768.

Horedt, G. P., & Neukum, G. (1984). Cratering rate over the surface of a synchronous satellite. *Icarus*, *60*(3), 710–717. https://doi.org/10.1016/0019-1035(84)90175-1

Hughes, D. W., & Williams, I. P. (2000). The velocity distributions of periodic comets and stream meteoroids. *Monthly Notices of the Royal Astronomical Society*, *315*(3), 629–634. https://doi.org/10.1046/j.1365-8711.2000.03435.x

Ito, T., & Malhotra, R. (2010). Asymmetric impacts of near-Earth asteroids on the moon. *Astronomy and Astrophysics*, *519*, A63. https://doi.org/10.1051/0004-6361/200912901

Kawamura, T., Morota, T., Kobayashi, N., & Tanaka, S. (2011). Cratering asymmetry on the moon: New insight from the Apollo passive seismic experiment. *Geophysical Research Letters*, *38*, L15201. https://doi.org/10.1029/2011GL048047

Kneissel, T., van Gasselt, S., & Neukum, G. (2011). Map-projection-independent crater size–frequency determination in GIS environments—New software tool for ArcGIS. *Planetary and Space Science*, *59*(11-12), 1243–1254. https://doi.org/10.1016/j.pss.2010.03.015

Korotev, R. L. (2005). Lunar geochemistry as told by lunar meteorites. *Chemie der Erde*, *65*(4), 297–346. https://doi.org/10.1016/j.chemer.2005.07.001

Le Feuvre, M., & Wieczorek, M. A. (2008). Nonuniform cratering of the terrestrial planets. *Icarus*, *197*(1), 291–306. https://doi.org/10.1016/j.icarus.2008.04.011

Le Feuvre, M., & Wieczorek, M. A. (2011). Nonuniform cratering of the moon and a revised crater chronology of the inner solar system. *Icarus*, *214*(1), 1–20. https://doi.org/10.1016/j.icarus.2011.03.010

Lorenzetti, S., Busemann, H., & Eugster, O. (2005). Regolith history of lunar meteorites. *Meteoritics and Planetary Science*, *40*(2), 315–327. https://doi.org/10.1111/j.1945-5100.2005.tb00383.x

Lucey, P. G., Costello, E. S., Ghent, R. R., & Li, S. (2018). Ice distribution at the poles of the Moon and Mercury: The role of regolith overturn. *Lunar and Planetary Science Conference*, *49th*, abstract #1678.

Mahan, R., (1991). Circular statistical methods: Applications in spatial and temporal performance analysis. Special report, *U.S. Army Research Institute for the Behavioral and Social Sciences*.

Mainzer, A., Grav, T., Bauer, J., Masiero, J., McMillan, R. S., Cutri, R. M., et al. (2011). NEOWISE observations of near-Earth objects: Preliminary results. *The Astrophysical Journal*, *743*(2), 156. https://doi.org/10.1088/0004-637X/743/2/156

Margot, J.-L., Pravec, P., Taylor, P., Carry, B., & Jacobson, S. (2015). Asteroid systems: Binaries, triples, and pairs. In P. Michel, F. E. DeMeo, & W. F. Bottke (Eds.), *Asteroids IV*, (pp. 335–374). Tucson, AZ: Univ. of Arizona Press. https://doi.org/10.2458/azu_uapress_9780816532131-ch019

McEwen, A. S., & Bierhaus, E. B. (2006). The importance of secondary cratering to age constraints on planetary surfaces. *Annual Review of Earth and Planetary Sciences*, *34*(1), 535–567. https://doi.org/10.1146/annurev.earth.34.031405.125018

McEwen, A. S., Preblich, B. S., Turtle, E. P., Artemieva, N. A., Golombek, M. P., Hurst, M., et al. (2005). The rayed crater Zunil and interpretations of small impact craters on Mars. *Icarus*, *176*(2), 351–381. https://doi.org/10.1016/j.icarus.2005.02.009

Mendell, W. W., & Low, F. J. (1974). Preliminary results of the Apollo 17 infrared scanning radiometer. *The Moon*, *9*(1-2), 97–103. https://doi.org/10.1007/BF00565396

Mendell, W. W., & Low, F. J. (1975). Infrared orbital mapping of lunar features. *Lunar and Planetary Science Conference Proceedings*, *9*, 2711–2719.

Michael, G. G., & Neukum, G. (2010). Planetary surface dating from crater size–frequency distribution measurements: Partial resurfacing events and statistical age uncertainty. *Earth and Planetary Science Letters*, *294*(3-4), 223–229. https://doi.org/10.1016/j.epsl.2009.12.041

Michel, P., & Froeschlé, C. (1997). The location of linear secular resonances for semimajor axes smaller than 2 AU. *Icarus*, *128*(1), 230–240. https://doi.org/10.1006/icar.1997.5727

Morota, T., & Furumoto, M. (2003). Asymmetrical distribution of rayed craters on the moon. *Earth and Planetary Science Letters*, *206*(3-4), 315–323. https://doi.org/10.1016/S0012-821X(02)01111-1

Morota, T., Haruyama, J., Honda, C., Yokota, Y., Ohtake, M., & Furumoto, M. (2008). Lunar apex antapex cratering asymmetry as an impactor recorder in the Earth moon system. *Advances in Space Research*, *42*(2), 285–288. https://doi.org/10.1016/j.asr.2007.05.055

Morota, T., Ukai, T., & Furumoto, M. (2005). Influence of the asymmetrical cratering rate on the lunar cratering chronology. *Icarus*, *173*(2), 322–324. https://doi.org/10.1016/j.icarus.2004.08.016

Morris, R. V. (1978). In situ reworking (gardening) of the lunar surface: Evidence from the Apollo cores. *Lunar and Planetary Science Conference Proceedings*, *9*, 1801–1811.

Neukum, G., Ivanov, B. A., & Hartmann, W. K. (2001). Cratering records in the inner solar system in relation to the lunar reference system. *Space Science Reviews*, *96*(1/4), 55–86. https://doi.org/10.1023/A:1011989004263

Oberbeck, V. R., & Morrison, R. M. (1973). On the formation of the lunar herringbone pattern. *Proceedings of the Lunar Science Conference*, *4*, 107–123.

Oberst, J., Christou, A., Suggs, R., Moser, D., Daubar, I. J., McEwen, A. S., et al. (2012). The present-day flux of large meteoroids on the lunar surface—A synthesis of models and observational techniques. *Planetary and Space Science*, *74*(1), 179–193. https://doi.org/10.1016/j.pss.2012.10.005

Ostrach L. R., Robinson M. S., Denevi B. W., & Thomas P. C. (2011). Effects of incidence angle on crater counting observations. *Lunar and Planetary Science Conference*, *42nd*, abstract #1202.

Paige, D. A., Foote, M. C., Greenhagen, B. T., Schofield, J. T., Calcutt, S., Vasavada, A. R., et al. (2010). The Lunar Reconnaissance Orbiter Diviner Lunar Radiometer Experiment. *Space Science Reviews*, *150*(1-4), 125–160. https://doi.org/10.1007/s11214-009-9529-2

Plescia, J. B., Robinson, M. S., Wagner, R., & Baldridge, R. (2016). Ranger and Apollo S-IVB spacecraft impact craters. *Planetary and Space Science*, *124*, 15–35. https://doi.org/10.1016/j.pss.2016.01.002

Powell, T. M., Greenhagen, B. T., Taylor, S., Williams, J.-P., Hayne, P. O., & Paige, D. A. (2018). Lunar cold spot properties and degradation. *Lunar and Planetary Science Conference*, 49th, abstract #1829.

Robinson, M. S., Brylow, S. M., Tschimmel, M., Humm, D., Lawrence, S. J., Thomas, P. C., et al. (2010). Lunar Reconnaissance Orbiter Camera (LROC) instrument overview. *Space Science Reviews*, *150*(1-4), 81–124. https://doi.org/10.1007/s11214-010-9634-2

Schunová, E., Jedicke, R., Walsh, K. J., Granvik, M., Wainscoat, R. J., & Haghighipour, N. (2014). Properties and evolution of NEO families created by tidal disruption at Earth. *Icarus*, *238*, 156–169. https://doi.org/10.1016/j.icarus.2014.05.006

Schunová-Lilly, E., Jedicke, R., Vereš, P., Denneau, L., & Wainscoat, R. J. (2017). The size-frequency distribution of $H > 13$ NEOs and ARM target candidates detected by pan-STARRS1. *Icarus*, *284*, 114–125. https://doi.org/10.1016/j.icarus.2016.11.010

Shoemaker, E. M. (1962). Interpretation of lunar craters. In Z. Kopal (Ed.), *Physics and Astronomy of the Moon*, (pp. 283–359). New York, NY: Academic Press.

Shoemaker, E. M. (1965). Preliminary analysis of the fine structure of the lunar surface in Mare Cognitum. In W. N. Heiss, D. R. Menzel, & J. A. O'Keefe (Eds.), *The nature of the lunar surface*, (pp. 23–77). Baltimore, Maryland: Johns Hopkins Univ. Press.

Shoemaker, E. M., & Wolfe, R. A. (1982). Cratering timescales for the Galilean satellites. In D. Morrison (Ed.), *Satellites of Jupiter*, (pp. 277–339). Tucson, AZ: Univ. of Arizona Press.

Speyerer, E. J., Povilaitis, R. Z., Robinson, M. S., Thomas, P. C., & Wagner, R. V. (2016). Quantifying crater production and regolith overturn on the moon with temporal imaging. *Nature*, *538*(7624), 215–218. https://doi.org/10.1038/nature19829

Stöffler, D., & Ryder, G. (2001). Stratigraphy and isotope ages of lunar geologic units: Chronological standard for the inner solar system. *Space Science Reviews*, *96*(1/4), 9–54. https://doi.org/10.1023/A:1011937020193

Vasavada, A. R., Bandfield, J. L., Greenhagen, B. T., Hayne, P. O., Siegler, M. A., Williams, J.-P., & Paige, D. A. (2012). Lunar equatorial surface temperatures and regolith properties from the Diviner Lunar Radiometer Experiment. *Journal of Geophysical Research*, *117*, E00H18. https://doi.org/10.1029/2011JE003987

Vasavada, A. R., Paige, D. A., & Wood, S. E. (1999). Near-surface temperatures on mercury and the moon and the stability of polar ice deposits. *Icarus*, *141*(2), 179–193. https://doi.org/10.1006/icar.1999.6175

Vondrak, R., Keller, J., Chin, G., & Garvin, J. (2010). Lunar Reconnaissance Orbiter (LRO): Observations for lunar exploration and science. *Space Science Reviews*, *150*(1-4), 7–22. https://doi.org/10.1007/s11214-010-9631-5

Wagner, R. V., Nelson, D. M., Plesia, J. B., Robinson, M. S., Speyerer, E. J., & Mazarico, E. (2017). Coordinates of anthropogenic features on the moon. *Icarus*, *283*, 92–103. https://doi.org/10.1016/j.icarus.2016.05.011

Warren, P. (1994). Lunar and Martian meteorite delivery service. *Icarus*, *111*(2), 338–363. https://doi.org/10.1006/icar.1994.1149

Werner, S. C., & Medvedev, S. (2010). The lunar rayed-crater population—Characteristics of the spatial distribution and ray retention. *Earth and Planetary Science Letters*, *295*(1-2), 147–158. https://doi.org/10.1016/j.epsl.2010.03.036

Williams, J.-P. (2018). Modification of the Martian surface by impact cratering. In R. Soare, S. Conway, & S. Clifford (Eds.), *Dynamic Mars: Recent and Current Landscale Evolution of the Red Planet*, (pp. 363–386). Amsterdam, Netherlands: Elsevier. https://doi.org/10.1016/B978-0-12-813018-6.00012-1

Williams, J.-P., Bandfield, J. L., Paige, D. A., Greenhagen, B. T., Speyerer, E. J., & Ghent, R. R., (2017). A recent, large multi-impact event on the Moon. *Lunar and Planetary Science Conference*, *48th*, abstract #2637.

Williams, J.-P., Bandfield, J. L., Paige, D. A., Powell, T. , Taylor, S., Hayne, P. O., et al. (2018). Large lunar cold spots: Ages and distribution. *Lunar and Planetary Science Conference*, *49th*, abstract #2275.

Williams, J.-P., Paige, D. A., Greenhagen, B. T., & Sefton-Nash, E. (2017). The global surface temperatures of the moon as measured by the Diviner Lunar Radiometer Experiment. *Icarus*, *283*, 300–325. https://doi.org/10.1016/j.icarus.2016.08.012

Williams, J.-P., Pathare, A. V., & Aharonson, O. (2014). The production of small primary craters on Mars and the moon. *Icarus*, *235*, 23–36. https://doi.org/10.1016/j.icarus.2014.03.011

Williams, J.-P., Sefton-Nash, E., & Paige, D. A. (2016). The temperatures of Giordano Bruno crater observed by the Diviner Lunar Radiometer Experiment: Application of an effective field of view model for a point-based data set. *Icarus*, *273*, 205–213. https://doi.org/10.1016/j.icarus.2015.10.034

Williams, J.-P., van der Bogert, C. H., Pathare, A. V., Michael, G. G., Kirchoff, M. R., & Hiesinger, H. (2018). Dating very young planetary surfaces from crater statistics: A review of issues and challenges. *Meteoritics and Planetary Science*, *53*(4), 554–582. https://doi.org/10.1111/maps.12924

Wood, J. A. (1973). Bombardment as a cause of the lunar asymmetry. *The Moon*, *8*(1-2), 73–103. https://doi.org/10.1007/BF00562751

Zahnle, K., Dones, L., & Levinson, H. F. (1998). Cratering rates on the Galilean satellites. *Icarus*, *136*(2), 202–222. https://doi.org/10.1006/icar.1998.6015

Zahnle, K., Schenk, P., Sobieszczyk, S., Dones, L., & Levison, H. F. (2001). Differential cratering of synchronously rotating satellites by ecliptic comets. *Icarus*, *153*(1), 111–129. https://doi.org/10.1006/icar.2001.6668

Zanetti, M., Stadermann, A., Jolliff, B., Hiesinger, H., van der Bogert, C. H., & Plescia, J. (2017). Evidence for self-secondary cratering of Copernican-age continuous ejecta deposits on the moon. *Icarus*, *298*, 64–77. https://doi.org/10.1016/j.icarus.2017.01.030

Zar, J. (1984). *Biostatistical Analysis*. Englewood Cliffs, NJ: Prentice-Hall, Inc.